Journal of Materials Chemistry C

ROYAL SOCIETY OF CHEMISTRY

PAPER

View Article Online
View Journal

Cite this: DOI: 10.1039/d2tc00477a

Temperature dependent local structure coherence of surface-modified $BaTiO_3$ nanocubes†

Bo Jiang, [a] Changhao Zhao, [bc] Peter C. Metz, [a] Palani Raja Jothi, [d] Benard Kavey, [e] Linda Reven, [f] Michael Lindner-D'Addario, [f] Jacob L. Jones, [c] Gabriel Caruntu [eg] and Katharine Page *[ad]

Received 2nd February 2022,
Accepted 20th April 2022

DOI: 10.1039/d2tc00477a

rsc.li/materials-c

Surface functionalized barium titanate ($BaTiO_3$) nanocrystals have been explored for highly tunable chemical and electronic properties, potentially of use in ceramic-polymer composites for flexible ferroelectric device applications, directed synthesis of ferroelectric thin films or other nano-architectures, and other potential applications. The detailed temperature dependent local structure evolution of $BaTiO_3$ nanocubes capped with nonpolar oleic acid (OA) and polar tetrafluoroborate (BF_4^-) ligands are investigated using *in situ* synchrotron X-ray diffraction and pair distribution function (PDF) analysis, in conjunction with piezoresponse force microscopy (PFM) and ^{137}Ba nuclear magnetic resonance (NMR) spectroscopy measurements. Diffraction analysis reveals that nanocubes capped by polar BF_4^- ligands undergo sharper ferroelectric to paraelectric phase transitions than nanocubes capped with nonpolar OA ligands, with the smallest ~12 nm nanocubes displaying no transition. Local non-centrosymmetric symmetry is observed by PDF analysis and confirmed by NMR, persisting across the phase transition temperature. Local distortion analysis, manifested in tetragonality (c/a) and Ti off-centering (z_{Ti}) parameters, reveals distinct temperature and length-scale dependencies with particle size and capping group. Ferroelectric order is increased by polar BF_4^- ligands, which is corroborated by an enhancement of PFM response.

1 Introduction

Functional $BaTiO_3$ nanocrystals have attracted considerable attention in recent years due to their multifunctional properties and environmentally friendly composition.[1] In particular, the tunable electronic and optical properties in ferroelectric $BaTiO_3$ nanocomposites provide the potential for energy storage and photovoltaic applications.[2–4] As the canonical lead-free ferroelectric material, the bulk $BaTiO_3$ adopts an average tetragonal $P4mm$ structure at ambient temperature, and undergoes a phase transition to a paraelectric cubic phase at the Curie temperature (T_C) of 393 K.[5] It is well known that physical and chemical properties of functional materials can be effectively tuned through strategies such as size reduction, shape control, bulk chemical substitution, and surface modification.[1,6–10] A plethora of experimental observations indicates that ferroelectric properties can diminish as particle sizes are reduced and some of them demonstrate a critical thickness or grain size.[11–19] Bulk structural probes generally indicate a transition towards cubic-like crystal structures and decreased structural coherence for reduced particle sizes. First-principles calculations have been widely invoked to explain experimental observations of grain size and interface effects in nanoscale ferroelectrics.[10,20–28] Several studies have been published specifically investigating the relationships between particle size and phase selection and transition behaviors in $BaTiO_3$ particles.[13,16,29–35] Smith *et al.*,[29] studying spherical nanoparticles prepared solvothermally with narrow size distributions around 26, 45, and 70 nm, suggested an increasingly diffuse phase transition for smaller $BaTiO_3$ particles as evidenced by Raman spectroscopy and synchrotron XRD. While

[a] Neutron Scattering Division, Oak Ridge National Laboratory, Oak Ridge, Tennessee, 37831, USA
[b] Department of Materials and Earth Sciences, Technical University of Darmastadt, 64287 Darmstadt, Germany
[c] Department of Materials Science and Engineering, North Carolina State University, Raleigh, North Carolina 27695, USA
[d] Department of Materials Science and Engineering and Institute for Advanced Materials and Manufacturing, University of Tennessee, Knoxville, TN 37996, USA. E-mail: kpage10@utk.edu
[e] Department of Chemistry and Biochemistry, Central Michigan University, Mountain Pleasant, MI, 48859, USA
[f] Department of Chemistry, Centre québécois sur les matériaux fonctionnels/Quebec Centre for Advanced Materials (CQMF/QCAM), McGill University, Montreal, QC H3A 0C5, Canada
[g] Department of Electrical Engineering and Computer Science and MANSID Research Center, Stefan Cel Mare' University, 13, Universitatii St., Suceava, 720229, Romania

† Electronic supplementary information (ESI) available. See DOI: https://doi.org/10.1039/d2tc00477a

they found the average structure of nanoparticles in this size regime to be tetragonal, lattice parameters grow metrically more cubic, and pair distribution function (PDF) analysis revealed enhanced local titanium displacements with nanoparticle size reduction. These contradictory indicators of ferroelectric distortion were understood to indicate a decreased spatial coherence of dipoles relative to their bulk counterparts. However, smaller particles were not addressed in their report. Rabuffetti *et al.*[36] reported a cubic average structure *via* Rietveld analysis for sub-10 nm $BaTiO_3$ nanocrystals at room temperature prepared *via* a vapor diffusion sol-gel method, but suggested either a tetragonal *P*4*mm* space group or orthorhombic *Amm*2 space group best described their local symmetry. Shi *et al.*[32] showed in temperature-dependent studies of nanoparticles ranging in size from 10 nm to 500 nm, that small nanoparticles exhibit lower *c*/*a* values and more diffuse phase transitions, yet maintain (or exhibit higher) local Ti displacements. The largest particles in their study, by contrast, were found to mimic the temperature dependent structural trends of bulk $BaTiO_3$. More recently, Hao *et al.*[37] examined the structure of 4.5 nm $BaTiO_3$ nanoparticles prepared *via* a triethylene glycol sol method with X-ray PDF and Raman spectroscopy, observing a clear and spatially coherent non-centrosymmetric crystal structure at room temperature and a diffuse phase transition process across a wide temperature range. Thin film aggregates of the small nanoparticles exhibited second harmonic generation (SHG) response (even at 400 °C) and exhibited macroscopic polarization probed with Piezoelectric Force Microscopy (PFM).[37] Overall, the picture emerges that the nature and coherence of ferroelectric domains may vary among differently prepared small sized $BaTiO_3$ nanocrystals, with particles falling in specific size ranges exhibiting further variation in their respective local and average atomic structures and associated phase transition behaviors.

Surface functionalization of nanoparticles is used to improve their properties in composites and ensure better bonding with the polymer matrix,[38–40] or to facilitate oriented attachment of specific shapes during colloidal growth of thin films or other nanostructures.[39,41,42] Several experimental and theoretical studies have indicated that shape or adsorbate-induced effects can stabilize the ferroelectric state in small particles of $BaTiO_3$.[43–45] Polking *et al.*[40] confirmed a larger coherence length scale of tetragonal distortions in $BaTiO_3$ nanocubes than in nanospheres by synchrotron atomic PDF analysis, further demonstrated by aberration-corrected transmission electron microscopy enhanced with holographic polarization imaging. A first attempt for understanding the local dipoles and capping benzyloxy ligand groups in 5 nm $BaTiO_3$ nanoparticles was carried out using time-of-flight (TOF) neutron scattering by Page *et al.*,[46] which revealed local dipole-dipole correlations remain present, albeit with greatly reduced lengthscale. There have been few studies aimed at understanding how different surface ligands may affect the internal structure and inhibit or support the presence of ferroelectricity in small nanocrystals. We previously reported a combined neutron total scattering, Density Functional Theory (DFT), and *ab initio* molecular dynamics (AIMD) study to analyze the effect of surface ligand polarity on the atomic structure of various sizes of $BaTiO_3$ nanocubes at room temperature.[47] The local rhombohedral-like bonding environments and ferroelectric distortion lengthscales in nanoparticles of $BaTiO_3$ were directly observed due to the high sensitivity of neutron scattering to Ti–O correlations. Interestingly, the polar BF_4^- ligands are found to stabilize the correlation length scale of local rhombohedral distortions in ferroelectric nanoparticles relative to those decorated with nonpolar OA capping ligands. However, there remains uncertainty surrounding the ligand polarity effects on the ferroelectric phase transition, in particular in small size nanocubes.

In this work, the temperature evolution of the local and average structure of various sizes of $BaTiO_3$ nanocubes with nonpolar OA and polar BF_4^- capping ligands was investigated by high-energy synchrotron X-ray diffraction and total scattering techniques. Variation in nanocrystal size and ligand capping are found to give rise to distinctly different temperature trends in ferroelectric distortion measures, including tetragonality (*c*/*a*) and Ti off-centering. Piezoresponse force microscopy (PFM) and ^{137}Ba nuclear magnetic resonance (NMR) probes support the observations. Our results build on recent reports of robust ferroelectric and polarization switching behaviors in small $BaTiO_3$ nanoparticles,[37,40] highlighting the role and interplay of size and surface decoration in controlling their phase transitions and associated physical properties.

2 Experimental methods

Samples were synthesized *via* the solvothermal route described in references[3,41,48] to obtain ~12 nm, ~20 nm, and ~39 nm $BaTiO_3$ nanocubes. The as-synthesized $BaTiO_3$ nanocubes have OA capping ligands and can be suspended in a nonpolar solvent such as hexane. Half of each batch was separated and treated with a solution of nitrosonium tetrafluoroborate ($NOBF_4$) in dimethylformamide (DMF), which exchanges the surface ligands and transfers the $BaTiO_3$ nanocubes from the nonpolar to polar solvents.[3] Samples were washed with dilute acetic acid solution to remove $BaCO_3$ phase impurity and dried, forming nanocrystalline powders well-suited for diffraction and PDF analysis.[48] The two sets of particles are hereafter referred to as BTnc@OA and BTnc@BF_4^-, indicating those capped with nonpolar OA ligands and polar BF_4^-, respectively. Transmission electron microscopy (TEM) was performed with a Zeiss Libra 200 MC microscope TEM operated at a 200 kV.

The synchrotron X-ray total scattering patterns were collected for nanocubes at beamline 11-ID-B of the Advanced Photon Source at Argonne National Laboratory.[49] The samples were measured in spinning polyimide capillaries in transmission mode. Non-ambient data were measured using a hot air blower. An X-ray energy of 87.6 keV (λ = 0.1432 Å) was used and the diffraction patterns were measured on a PerkinElmer 2D detector. Total scattering data was collected with a sample-to-detector distance of approximately 245 mm, resulting in a

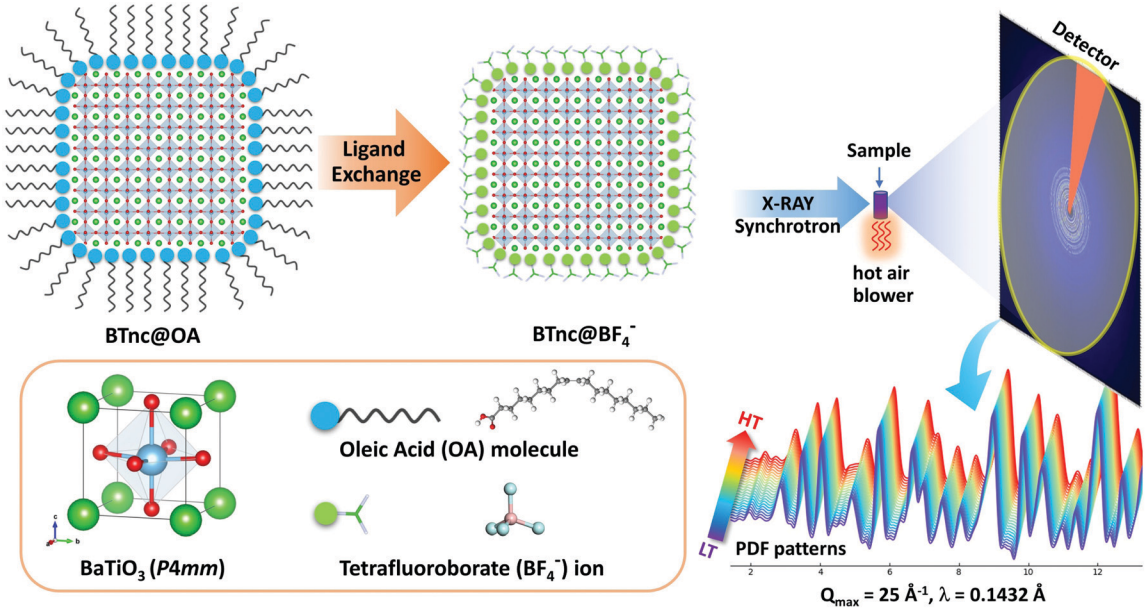

Fig. 1 Schematic diagram of the ligand-exchange process to synthesize $BaTiO_3$ ferroelectric oxide nanocubes in this work and experimental setup for high-energy synchrotron X-ray diffraction and PDF data measurement.

usable Q_{max} of 25 $Å^{-1}$. The 2D detector image was calibrated with a CeO_2 standard and corrected for X-ray polarization and geometrical aberations using Fit2D.[50] The resultant 1D total scattering pattern was converted to real-space using PDFgetX3, with r_{poly} values of 0.8 Å (more aggressive r_{poly} filters were found to improve adherence to the theoretical $-4\pi\rho r$ baseline of the PDF function, yet were not applied since they were found to have minimal impact within our fitting range, above 1.8 Å in r).[51] Rietveld and PDF refinements were performed using TOPAS v6 Academic[52] software. Four known crystallographic phases of $BaTiO_3$ (cubic $Pm\bar{3}m$, tetragonal $P4mm$, orthorhombic $Amm2$, and ground state rhombohedral $R3m$) were tried as models for Rietveld and PDF refinements of the samples.[5] In these PDF refinements, a numerical shape function developed for cube-shaped nanoparticles[53] was applied. This numerical approach provides a physically accurate model for the size and shape of the nanoparticles, as shown in Fig. S1 (ESI†). A schematic of the samples synthesized and synchrotron X-ray total scattering measurements completed is shown in Fig. 1.

Dual AC Resonance Tracking piezoresponse force microscopy (DART-PFM) and switching spectroscopy PFM (SS-PFM) were carried out on an MFP-3D system from Asylum Research for an ~20 nm BTnc@OA and ~20 nm BTnc@BF4-nanocube sample set, as well as a larger ~100 nm BTnc@OA nanocube. DART-PFM measurements were performed using a platinum/titanium coated cantilever (AC240TM, nominal spring constant of 2 N m^{-1} and a resonance frequency of 70 kHz). Unlike other piezoresponse techniques, in the dual AC resonance tracking method the potential of the conductive cantilever is the sum of two oscillating voltages, one corresponding to a frequency below resonance and the other to a frequency above resonance. The precise measurement of the amplitudes at these two frequencies enables the user to track the resonant frequency, thereby improving substantially the signal to noise ratio and the resolution of the measurement. This allows for reproducible imaging over an extended period of time and for decoupling the surface topography from the measured PFM signal, thereby eliminating crosstalk effects.[54–56] The Olympus AC240TM conductive microcantilever was used to excite the sample with a small oscillating voltage, V_{tip},

$$V_{tip} = V_{dc} + V_{ac}\cos(\omega t) \quad (1)$$

with the amplitude of 40 mV. The alternating current generated by the tip will polarize the ferroelectric layer, inducing its deformation due to the converse piezoelectric effect. The photodetector signal amplitude generated by the elastic deformation of the piezoelectric layer was demodulated with two separated lock-in amplifiers and the values of the piezoelectric coefficient were obtained after calibrating the photodetector signal. Since the piezoresponse of the sample is described as the first harmonic component of the tip deflection:

$$A = A_0 + A_{1\omega}\cos(\omega t + \varphi) \quad (2)$$

the phase φ provides information about the orientation of the electrical dipoles, whereas the amplitude $A_{1\omega}$ describes the electromechanical properties of the material.

Wideline ^{137}Ba NMR spectra were acquired for nanocubes at resonance frequencies of 44.47 and 55.58 MHz on Varian 400 MHz and Bruker 600 MHz NMR spectrometers respectively using a Hahn echo pulse sequence. Acquisition times of 16 hours were required due to the limited amount of material and the low NMR sensitivity of the ^{137}Ba isotope. The line shape deconvolutions were performed using Bruker TopSpin v4 Software to extract the quadrupole coupling constant C_Q. For the central transition ($m = 1/2 \leftrightarrow m = -1/2$) of ^{137}Ba, $I = 3/2$, the peaks were fit over the range of the peak center plus or minus

the full width at half maximum (FWHM). For the ordered component, assumed to be a tetragonal quadrupole line shape, the asymmetry parameter, η, was set to 0 with minimal line broadening of 100 Hz. For the disordered component, η = 0 with 100 Hz line broadening and the quadrupole coupling constant C_Q was set to 0.

3 Results and discussion

$BaTiO_3$ is well known to have a tetragonal *P4mm* perovskite average structure at room temperature, transitioning to a cubic phase average structure above ~393 K. Leading up to the transition, the longer *c* lattice parameter is reduced and the shorter *a* lattice parameter is lengthened; there is a single cubic lattice parameter *a* above the transition. We first performed Rietveld refinements of all synchrotron X-ray diffraction data from the three particle size samples using the tetragonal *P4mm* phase model, and the temperature dependencies of the resulting lattice parameters are shown in Fig. 2(a–c). The room temperature data is indexed in all cases with a single tetragonal *P4mm* phase. Rietveld refinements are shown in Fig. S2 (ESI†). The insets in Fig. S2 (ESI†) show collected temperature dependent patterns from 300 K to 440 K, revealing no significant changes with increasing temperature for any of the samples. TEM images in Fig. 2(d–f) shows the cube-like shapes for ~39 nm and ~20 nm nanocubes, and more sphere-like shapes for particles with size ~12 nm, as reported in our previous work.[47]

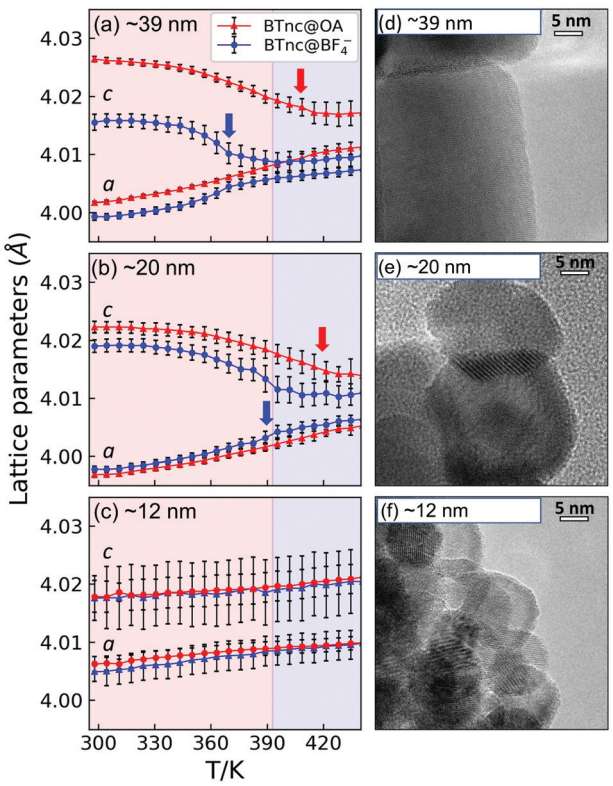

Fig. 2 Lattice parameters resulting from Rietveld refinement of 300 K to 440 K X-ray diffraction data using a *P4mm* model phase for average $BaTiO_3$ nanocube sizes of (a) ~39 nm, (b) ~20 nm and (c) ~12 nm. The color boundary shows the phase transition temperature of bulk $BaTiO_3$ while arrows have been added to call attention to inflection points in the nanocube data, indicating the temperature regimes of the diffuse phase transitions of the $BaTiO_3$ nanocubes. (d–f) show the high resolution TEM images corresponding to the various particle size samples.

The *a* and *c* lattice parameters of the larger two sizes of nanocubes show overall similar trends, gradually approaching a single value at higher temperatures and indicating diffuse crystallographic phase transitions. The trends indicate a phase transition for ~39 nm BTnc@BF_4^- at ~370 K and for ~20 nm BTnc@BF_4^- at ~390 K, which is lower (albeit more distinct) than that for ~39 nm BTnc@OA at ~410 K and ~20 nm BTnc@OA at ~420 K. No evidence for a crystallographic phase transition is observed for the smallest ~12 nm nanocubes up to 450 K. This result suggests that the average structure of smallest ~12 nm $BaTiO_3$ nanocubes is close to being metrically cubic (due to lower *c*/*a* values and large error bars), with the phase transition suppressed entirely over the range of temperatures investigated and the ligand exchange having no significant impact. We note the observed lattice parameter trends are consistent with the tetragonal symmetry uncovered far above the bulk $BaTiO_3$ phase transition in 4.5 nm monodomain particles by Raman spectroscopy.[37] It is notable, however, for larger nanocubes, the polar BF_4^- capped ligands result in less diffuse, lower temperature phase transitions, and even a significant reduction in the observed average lattice parameter. This may correlate with a greater degree of structural coherence (or fewer surface ligand induced defects) in the ~39 nm and ~20 nm BF_4^- capped particles, with OA capped particles and ~12 nm nanocubes studied here comparatively disordered. This idea is discussed further with the analysis of PDF data below.

PDF analysis of synchrotron X-ray data was carried out to characterize the local symmetry and the correlation length scales for dipole ordering for all nanoparticles. Fig. 3(a) shows PDF patterns of various size and ligand capped $BaTiO_3$ nanocubes at 300 K with 1–80 Å distance range. The amplitude of PDF peaks at larger distances is seen to increase with the increase in particle size. The highest pair correlations visible for nanocubes with ~12 nm, ~20 nm, and ~39 nm are ~60 Å, ~65 Å, and ~70 Å (~6–7 nm). This is much lower than actual crystallographic domain sizes due in part to the low reciprocal-space resolution and corresponding dampening of the PDF at high *r*, though the trend clearly correlates with particle size. Our previous neutron PDFs[47] (which offer far less instrument dampening of the PDF at high *r*) fitted with an analytical cube shape function[53] yielded coherent domain sizes smaller than particle sizes observed by TEM analysis, which indicates structural coherence loss or multiple domains existing in the particles. These findings of structural coherence loss have been reported by other synchrotron PDF studies on 5–10 nm $BaTiO_3$ nanocrystals[36,57,58] and depart from the monodomain structure recently observed in 4.5 nm particles.[37]

The PDF patterns of the four known crystallographic phases of $BaTiO_3$ are simulated and shown in Fig. 3(b) for comparison.

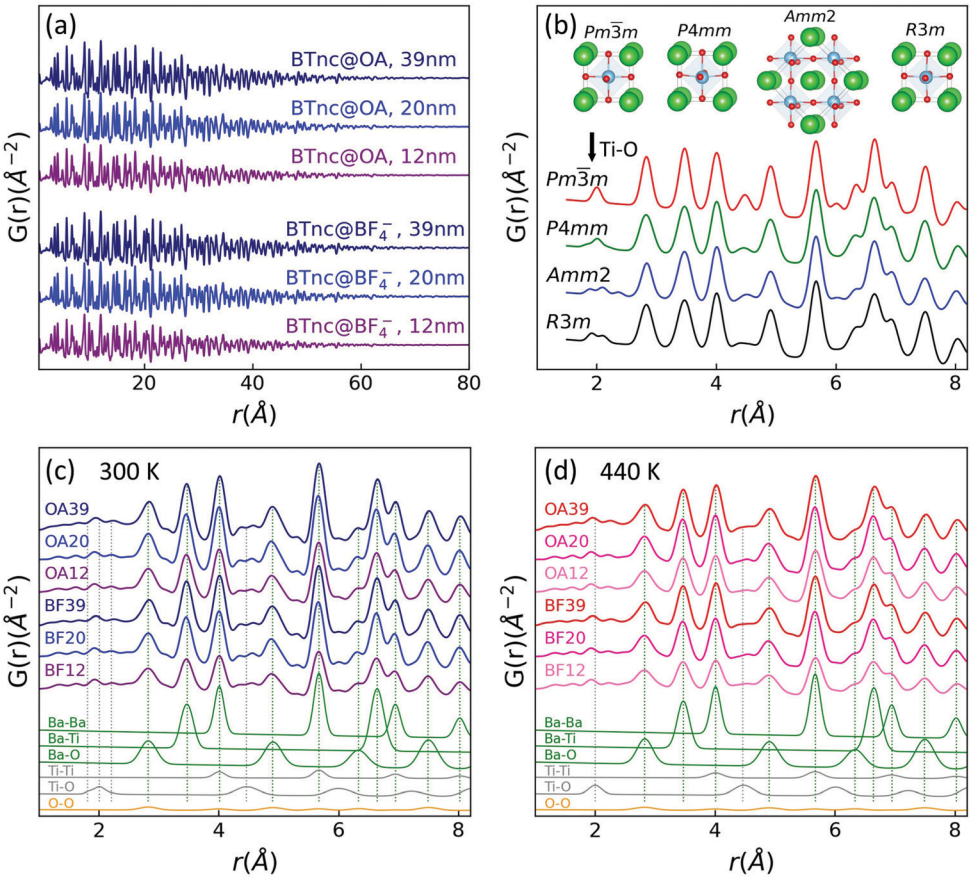

Fig. 3 (a) Comparison of the $G(r)$ for different $BaTiO_3$ nanocubes over 80 Å distance range. (b) Calculated PDFs from four crystallographic phases (cubic $Pm\bar{3}m$, tetragonal $P4mm$, orthorhombic $Amm2$ and rhombohedral $R3m$) with a fixed U_{iso} value = 0.005 Å^2 for all atoms, with corresponding models shown above. (c and d) The experimental local r range PDFs at 300 K and 440 K, along with simulated partial PDFs computed from $P4mm$ and $Pm\bar{3}m$ models, respectively.

There are distinct features in the nearest neighbor PDF peak, corresponding to the Ti–O pair distances in each TiO_6 octahedron. There is one distance for the six Ti–O bonds and therefore one well-defined PDF peak for the centrosymmetric cubic phase, and a broad peak (composed of one short, four medium and one long Ti–O distances) for the non-centrosymmetric tetragonal phase. The non-centrosymmetric orthorhombic $Amm2$ and rhombohedral $R3m$ models have three and two visible Ti–O peaks at $\sim$2 Å due to their unique TiO_6 octahedral distortions, respectively. In the experimental PDFs at 300 K and 440 K, shown in Fig. 3(c) and (d), it is difficult to determine the symmetry of the local bonding environment due to the relatively low intensity of the X-ray PDF Ti–O peaks and the presence of Fourier noise. The fitted 300 K PDF model using the tetragonal $P4mm$ phase in Fig. 3(c) and 440 K PDF model using the cubic $Pm\bar{3}m$ phase in Fig. 3(d) are decomposed into their respective partial PDFs below the experimental data, with vertical dashed lines providing guides to the eye for model pair correlations. We note the slight mismatch for the Ti–O peaks between the experimental PDFs and tetragonal and cubic model PDFs, which differs from the conclusion of local tetragonal symmetry found for 5 nm spherical nanocrystalline $BaTiO_3$ by Petkov *et al.*[57] This is the primary reason neutron PDFs were used in previous work on bulk[59] and nanocrystalline[47] $BaTiO_3$ to confirm the rhombohedral local bonding environment found across all phase transitions.

Temperature dependent PDF $G(r)$ up to r = 20 Å are displayed in Fig. S3 (ESI†). No abrupt changes or extra peaks are observed in the samples over the temperature range probed, though peaks are broadened at higher temperatures due to increases in atomic thermal vibration. To examine the details of local and intermediate range structure, the PDFs of the various size $BaTiO_3$ nanocubes capped with OA and BF_4^- at 300 K and 400 K were refined over the local (1.5–10 Å) and intermediate (10–50 Å) range. Fig. 4 shows the PDF refinement results for the smallest $\sim$12 nm nanocubes using each of the four known crystallographic phases of $BaTiO_3$; analyses for the larger size nanocubes are shown in Fig. S4 and S5 (ESI†). The refinement R_w factors and atomic displacement parameters (ADP) for Ti atoms resulting from applying each of the four crystallographic phase models are summarized in Tables S1 and S2 (ESI†) for all nanoparticles, respectively. Similar analytics have been applied to evaluate the structure of $BaTiO_3$ nanocrystals with X-ray PDF analysis in the past,[9,32,36,37] however the referenced studies did not draw a distinction between non-centrosymmetric tetragonal and orthorhombic models. The recent work by Hao *et al.*[37]

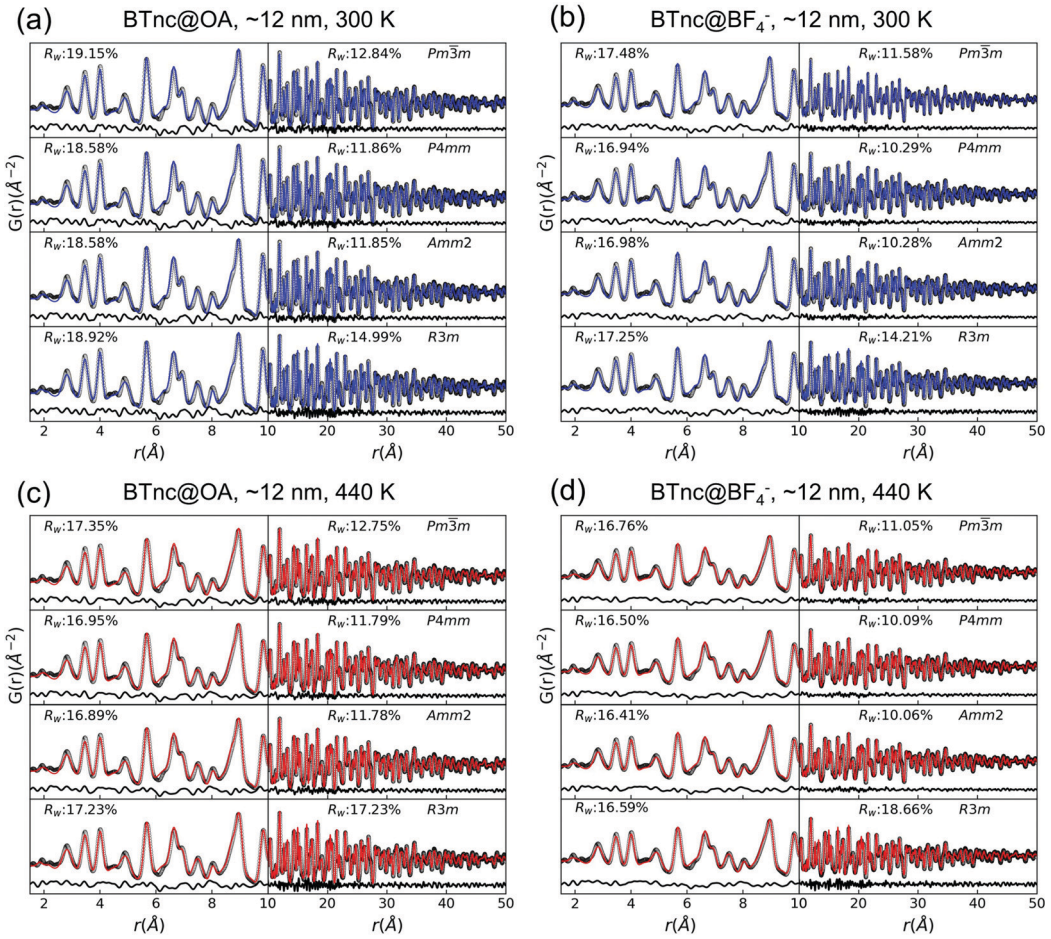

Fig. 4 PDF refinements of synchrotron X-ray data using centrosymmetric cubic *Pm*$\bar{3}$*m*, and non-centrosymmetric (tetragonal *P*4*mm*, orthorhombic *Amm*2 and rhombohedra *R*3*m*) at (a and b) 300 K and (c and d) 440 K for $BaTiO_3$ ~12 nm nanocubes with OA and BF_4^- ligand capping.

used in part the attainment of reasonable Ti isotropic atomic displacement parameter values to confirm non-centrosymmetric local structure in 4.5 nm monodomain particles, commenting on a similar quality of fit among the non-centrosymmetric models applied. Hao *et al.* did not examine any size- or fit-range dependent effects.

In this work, all four models result in visually similar fits and similar R_w values in Table S1 (ESI†), making it difficult to determine the nature of the distinct local structures from this data alone. Previous room temperature neutron PDF analysis work on the same series of samples[47] indicated rhombohedral local and orthorhombic intermediate-range order in $BaTiO_3$ nanocubes. This is consistent with the success of non-centrosymmetric phase models here over the 1.5–10 Å range, even at 440 K. For 10–50 Å fits, the non-centrosymmetric rhombohedral *R*3*m* model provides much worse fitting results compared to other phases, while the tetragonal phase model provides the best fit for larger nanocubes, and the orthorhombic phase model provides the best fit for the ~12 nm nanocubes. ADP values for Ti atoms provide further insight, with enlarged values indicating static or dynamic displacements of atoms farther from model crystallographic lattice sites. Models resulting in comparatively lower ADPs, in turn, indicate atom positions and motifs that better reflect the true atomic order of the system. The non-centrosymmetric orthorhombic *Amm*2 models result in the lowest values for the 10–50 Å range fits for all samples, while tetragonal *P*4*mm* models result in the lowest Ti ADP values for 1.5–10 Å fits for nearly all samples (the difference is within error for the smallest size samples). It is seen from our analysis that the polar BF_4^- ligand capping had little effect on the local and intermediate-range model selection, but corresponds with lower R_w values (better model agreement) for all conditions. Overall, our results for different *r* ranges suggest robust non-centrosymmetric phase stability during size reduction, maintained above the macroscopic phase transition temperatures.

Tetragonality (c/a) and Ti off-centering (z_{Ti}) parameter (in fractional atomic coordinate as ($0.5\text{-}z_{Ti}$)) in $BaTiO_3$ are known to strongly correlate with ferroelectric properties, being indicators of polarizability.[32,60,61] The thermal evolution of the c/a from various length-scale PDF modeling using non-centrosymmetric tetragonal *P*4*mm* model are compared to results from Rietveld refinements (Fig. 5). Note that the c/a ratio from local PDF refinement for all particles over the *r* range 1.5–20 Å (black

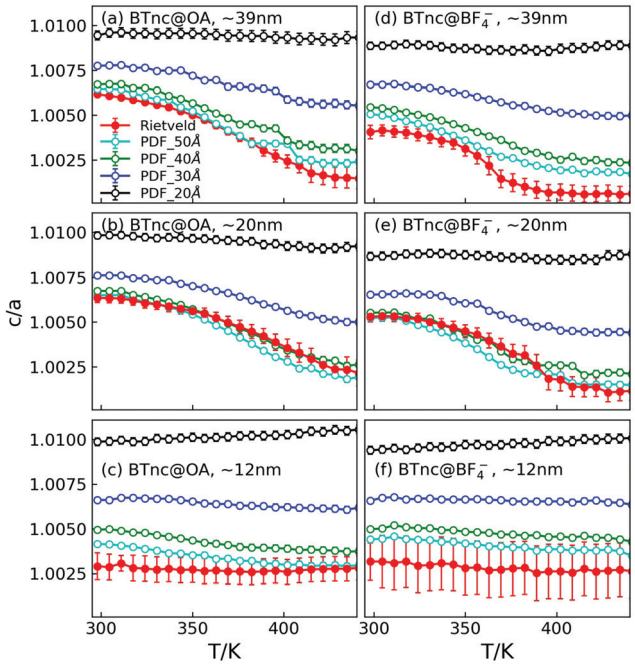

Fig. 5 Temperature dependence of tetragonality (c/a) ratios resulting from Rietveld and various real-space range PDF refinements for (a and d) ~39 nm, (b and e) ~20 nm, and (c and f) ~12 nm $BaTiO_3$ nanocubes capped with (a–c) OA and (d–f) BF_4^-.

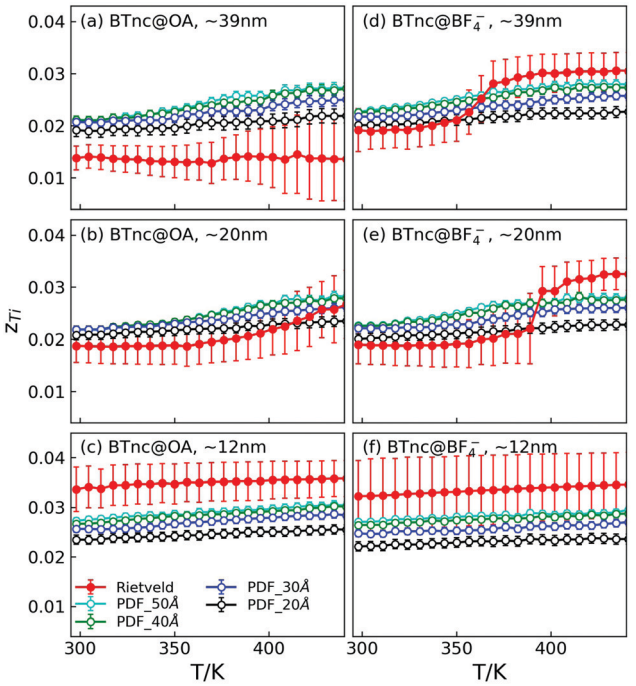

Fig. 6 Temperature dependence of z_{Ti} resulting from Rietveld and various real-space range PDF refinements for (a and d) ~39 nm, (b and e) ~20 nm, and (c and f) ~12 nm $BaTiO_3$ nanocubes capped with (a–c) OA and (d–f) BF_4^-.

circles) remains close to constant across all temperatures, which reveals that the particles have similar local structures for all sizes and temperatures. Increasing the window for refinement (the length-scale from 20 Å to 50 Å) results in decreased c/a ratio, especially at high temperature for ~20 nm and ~39 nm nanocubes. This indicates that the configurational disorder increased with fitting range and temperature. It is noteworthy that nonpolar ligand capping influences the temperature dependent behavior of ~20 and ~39 nm nanocrystals significantly *versus* polar ligand capping. This can be seen in the sharper transitions and lower c/a model ratios exhibited by polar BF_4^- capped nanocubes, relative to those of nonpolar OA capped nanocubes. As in the Rietveld results presented in Fig. 2 and shown as red spheres in Fig. 5, this tetragonality (c/a) remains approximately constant for the ~12 nm particles at all temperatures, apparently not influenced by the choice of ligand capping.

Similar trends are observed for the temperature and length-scale dependence of the Ti off-centering (z_{Ti}) parameter in the nanocube data, as shown in Fig. 6. An increasing z_{Ti} was observed for all nanocubes with increased refinement window (up to 50 Å), which is consistent with the analysis from Rabuffetti *et al.* and Smith *et al.*[29,36] Notably, in terms of local structure (PDF modeling results for different r range windows) the z_{Ti} parameter remains similar and is not strongly influenced by ligand capping, especially in ~12 nm particles. On the other hand, the large error values in z_{Ti} parameter from average structure modeling (Rietveld analysis) make it difficult to draw conclusions regarding the average behavior of the nanocubes. A transition in the z_{Ti} parameter is seen in polar ligand-capped ~20 and ~39 nm nanocubes (Rietveld analysis).

PDF refinements with variable r-range are often used to determine a length scale for local atomic departures from average structure motifs.[29,47,62] Fig. 7 compares the evolution of lattice parameters a and c with variable r-range at 300 K and 440 K. The corresponding goodness of fit R_w and Ti off-centering (z_{Ti}) parameters are shown in Fig. S6 and S7 (ESI†), respectively. For r_{max} larger than ~20 Å, a increases and c decreases with increasing fitting r-range, consistent with other literature.[36] Similar values for a and c were observed at ~20 Å for all nanocubes at 300 K and 440 K. Larger nanocubes show a reduction in tetragonality at high temperature, with only modest influence observed for the ~12 nm nanocubes. Overall, we note the specific model parameters resulting from our analysis are influenced by the choice of structure model and the data range over which it is applied. Nonetheless, the distinct trends observed for nonploar OA *versus* polar BF_4^- ligand capped particles robustly indicate their disparate nanoscale ordering effects and phase transition behaviors.

PFM experiments performed on individual 20 nm $BaTiO_3$ nanocubes capped with OA and BF_4^- have revealed the existence of a robust piezoelectric response at room temperature, which confirms the existence of a non-centrosymmetric structure in the $BaTiO_3$ nanocubes previously suggested by Raman spectroscopy and neutron diffraction experiments.[42,47] The averaged piezoresponse hysteresis loop analysis *via* PFM shown in Fig. 8(a) clearly suggests the presence of a hysteretic behavior in the phase signal of the surface capped $BaTiO_3$ nanocubes

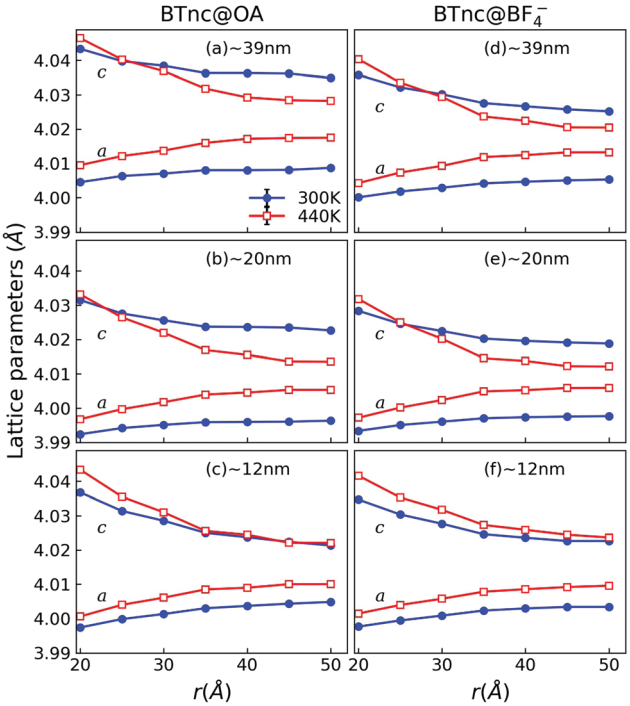

Fig. 7 The lattice parameters *a* and *c* resulting from PDF refinement with varying r_{max} range from 20 Å to 50 Å. Blue symbols correspond to 300 K data and red symbols correspond to 440 K data.

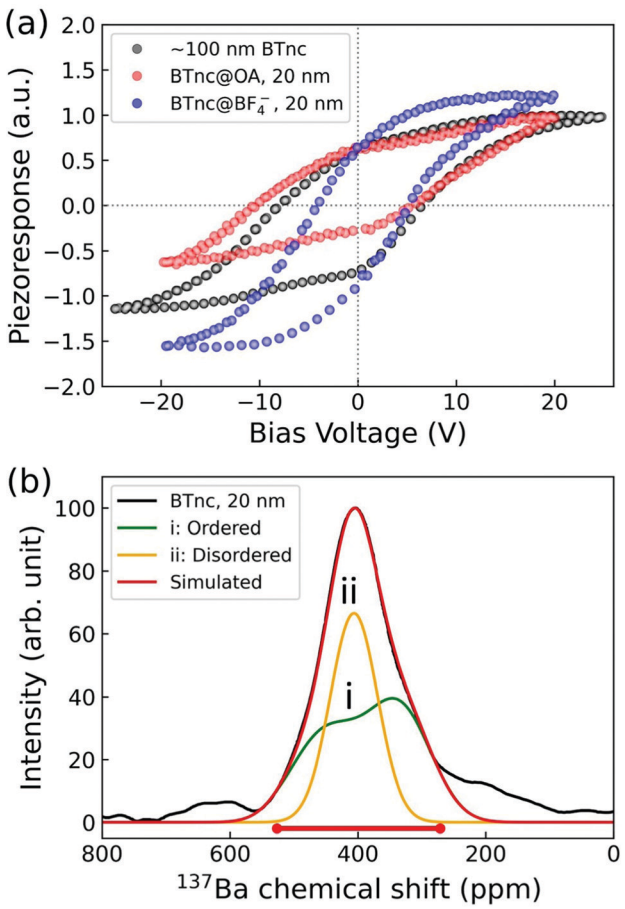

Fig. 8 (a) Normalized piezoresponse hysteresis loops of 20 nm $BaTiO_3$ nanocubes capped with OA and BF_4^- compared with the hysteresis loops of 100 nm $BaTiO_3$ nanocubes capped with OA. (b) Example deconvolution of ^{137}Ba NMR spectra (black). Curve i represents the ordered component (green line) and curve ii the disordered component (orange line). The red bar represents the range of the fitting algorithm.

with a 180° phase shift, as expected from the reversible shifting of the electric dipoles. An averaged value of the signals over a wide area was used to confirm that the hysteretic behavior is present over the whole sample and not only at a specific location.

It is interesting to note that the piezoelectric response of 20 nm $BaTiO_3$ nanocubes capped with OA is comparable with that of 100 nm $BaTiO_3$ nanocubes, whereas a visible enhancement of the PFM phase signal is observed in the case of the 20 nm $BaTiO_3$ nanocubes capped with BF_4^-. The hysteresis loop of OA capped particles shows a shift along the polarization axis, which is common in nanostructures due to effects of a depolarizing field, domain pinning, and regions that cannot be switched.[63,64] At the same time, the coercive field of 20 nm $BaTiO_3$ nanocubes capped with BF_4^- decreased markedly compared with the coercive fields of the OA capped 100 nm and 20 nm $BaTiO_3$ nanocubes, respectively. Such a behavior suggests that the replacement of OA molecules on the surface of the $BaTiO_3$ nanocubes with BF_4^- leads to an enhancement of the polar ordering in these nanocubes and a faster switching of the electric dipoles. This is a result of the local electric field created by the polar BF_4^- ions around the $BaTiO_3$ nanocubes, which leads to surface polarization screening (free charges compensate polarization bound charges at the particle interfaces that would otherwise act to destabilize the ferroelectric phase).[65]

Solid-state NMR studies have provided great insight into the structure of $BaTiO_3$.[66] The most common isotope of barium, ^{137}Ba, has a nuclear spin of 3/2 and possesses a quadrupole moment that will interact with the surrounding electric field gradient (EFG). The quadrupole coupling constant, C_Q, is proportional to the square of the spontaneous polarization and can be extracted from the line shape of the central transition ($m = 1/2 \leftrightarrow m = -1/2$) that is broadened by the second order quadrupole interaction. The ^{137}Ba quadrupole line shapes of the central transition of the four different crystal phases of BTO are distinct. The ^{137}Ba NMR spectrum of cubic phase ($>T_C$) is not broadened by the quadrupole interaction, $C_Q = 0$. ^{137}Ba NMR studies of single crystal and polycrystalline BTO[67] show that the tetragonal and rhombohedral ^{137}Ba quadrupole powder patterns are both axially symmetric (asymmetry parameter $\eta = 0$). The rhombohedral phase has a smaller quadrupole coupling constant (C_Q = 2.09 MHz at T = 160 K), than the tetragonal phase (C_Q = 2.86 MHz at T = 397 K). The ^{137}Ba quadrupole powder pattern of the orthorhombic phase on the other hand is highly asymmetric (η = 0.98) with C_Q = 2.20 MHz at T = 260 K.

In Fig. 8(b), the ^{137}Ba NMR spectrum of 20 nm BTnc@OA nanocubes was fitted to a core–shell model based on previous

studies of $BaTiO_3$ nanopowders[31,68,69] where the disordered surface sites give rise to a Gaussian component. As the particle size of the $BaTiO_3$ nanopowders is reduced, the disordered component, arising from a distribution of quadrupole couplings, becomes proportionally larger and dominates the ^{137}Ba NMR line shape. Based on this previous work, the ordered component of the nanocubes was assumed to be tetragonal, yielding a quadrupole coupling constant, C_Q 2.5 MHz at T = 298 K for both the BF_4^- and OA functionalized nanocubes. The fraction of the ordered component among nanocubes tested ranged from ~0.6 to 0.7. The ordered fraction for the BF_4^- stabilized nanocubes is slightly greater than that of the OA stabilized nanocubes, in agreement with diffraction and PDF analysis (though particle size differences or variation in local to long range symmetry would influence the results). Applying the core–shell model[31,68,69] and a cube shape particle morphology, the thickness of the disordered layer was estimated using the following equation:

$$\text{Thickness} = \frac{S}{2}(1 - \%O^{1/3}) \quad (3)$$

where S denotes the size of the nanocube, and $\%O$ represents the percent of the ordered component. Using S = 20 nm and $\%O$ = 0.7 from the BF_4^- stabilized nanocubes, the thickness is ~1 nm, in agreement with other $BaTiO_3$ nanopowder NMR studies.[31,68,69] The layer is slightly larger (~1.5 nm) for nanocubes with the fraction of ordered component ~0.6 (typical of OA particles in this study).

If the ordered component is alternatively taken to be strictly orthorhombic, the core–shell model becomes problematic. The maximum intensity of asymmetric orthorhombic ^{137}Ba quadrupolar line shape, located at the central singularity, coincides with the disordered Gaussian component at ~0 MHz. Our analysis does not exclude a local structure that is intermediate between tetragonal and orthorhombic, a gradient in the tetragonality, that would give rise to a ^{137}Ba quadrupole line shape with a smaller asymmetry parameter. Recent work on $BaTiO_3$ ceramic samples of various grain size[33] similarly observed that multiple phases are in coexistence. The PFM responses and NMR spectral analysis are thus consistent with increased coherence of internal BTnc@BF_4^- dipoles relative to those of BTnc@OA, and the possible coexistence of disparate symmetries throughout the nanocube volume, in agreement with our diffraction and PDF analyses.

4 Conclusions

In summary, the temperature evolution of the local and average structures of various sizes of $BaTiO_3$ nanocubes with nonpolar OA and polar BF_4^- ligand capping were investigated by high energy synchrotron X-ray total scattering. Rietveld and PDF refinements using various models demonstrated that the $BaTiO_3$ nanocubes present nominally identical non-centrosymmetric local structure for all sizes, including across observed average ferroelectric to paraelectric phase transitions. The symmetry of local and intermediate-range structures were observed to differ, varying with particle size and measurement temperature. The coexistence of disparate symmetries was confirmed by NMR spectral analysis. Introducing polar BF_4^- ligands was found to significantly alter measures of tetragonality in larger particles (above ~20 nm), resulting in a sharper and lower temperature phase transition behavior, increased structural coherence, and a greater PFM response. These temperature dependent findings demonstrate the importance of size and surface/interface modification in controlling the phase transitions and properties of ferroelectric nanoparticles.

Conflicts of interest

There are no conflicts to declare.

Acknowledgements

Structure analysis was supported by the U.S. Department of Energy (DOE), Office of Science, Office of Basic Energy Sciences Early Career Research Program Award KC040602 (PI: Page), supported by the Office of Science of the U.S. Department of Energy under Contract No. DE-AC05-00OR22725. This research used resources of the Advanced Photon Source, a U.S. Department of Energy (DOE) Office of Science User Facility, operated for the DOE Office of Science by Argonne National Laboratory under Contract No. DE-AC02-06CH11357. G. C. thanks the Office of Research and Graduate Studies at Central Michigan University and the Executive Agency for Higher Education, Research Development and Innovation Funding (Romania) through the grant No. PN-III-P4-ID-PCCF2016-0175. J. L. J. acknowledges support from the U.S. National Science Foundation under award number DMR-2004455.

Notes and references

1 M. Acosta, N. Novak, V. Rojas, S. Patel, R. Vaish, J. Koruza, G. Rossetti Jr and J. Rödel, *Appl. Phys. Rev.*, 2017, **4**, 041305.
2 M. Bi, Y. Hao, J. Zhang, M. Lei and K. Bi, *Nanoscale*, 2017, **9**, 16386–16395.
3 S. S. Parizi, A. Mellinger and G. Caruntu, *ACS Appl. Mater. Interfaces*, 2014, **6**, 17506–17517.
4 C. Won, Y. Park, K. Lee, H. Ryu and N. Hur, *J. Appl. Phys.*, 2011, **109**, 084108.
5 G. Kwei, A. Lawson, S. Billinge and S.-W. Cheong, *J. Phys. Chem. C*, 1993, **97**, 2368–2377.
6 M. A. El-Sayed, *Acc. Chem. Res.*, 2004, **37**, 326–333.
7 Y. Li, Z. Liao, F. Fang, X. Wang, L. Li and J. Zhu, *Appl. Phys. Lett.*, 2014, **105**, 182901.
8 C. W. Beier, M. A. Cuevas and R. L. Brutchey, *Langmuir*, 2010, **26**, 5067–5071.
9 J. Lombardi, L. Yang, F. A. Pearsall, N. Farahmand, Z. Gai, S. J. Billinge and S. O'Brien, *Chem. Mater.*, 2019, **31**, 1318–1335.

10 Z. Sun, L. Zhang, F. Dang, Y. Liu, Z. Fei, Q. Shao, H. Lin, J. Guo, L. Xiang and N. Yerra, *et al.*, *CrystEngComm*, 2017, **19**, 3288–3298.
11 K. Uchino, E. Sadanaga and T. Hirose, *J. Am. Ceram. Soc.*, 1989, **72**, 1555–1558.
12 B. D. Begg, E. R. Vance and J. Nowotny, *J. Am. Ceram. Soc.*, 1994, **77**, 3186–3192.
13 M. Frey and D. Payne, *Phys. Rev. B: Condens. Matter Mater. Phys.*, 1996, **54**, 3158.
14 S. Tsunekawa, S. Ito, T. Mori, K. Ishikawa, Z.-Q. Li and Y. Kawazoe, *Phys. Rev. B: Condens. Matter Mater. Phys.*, 2000, **62**, 3065.
15 Z. Zhao, V. Buscaglia, M. Viviani, M. T. Buscaglia, L. Mitoseriu, A. Testino, M. Nygren, M. Johnsson and P. Nanni, *Phys. Rev. B: Condens. Matter Mater. Phys.*, 2004, **70**, 024107.
16 T. Hoshina, H. Kakemoto, T. Tsurumi, S. Wada and M. Yashima, *J. Appl. Phys.*, 2006, **99**, 054311.
17 T. Hoshina, S. Wada, Y. Kuroiwa and T. Tsurumi, *Appl. Phys. Lett.*, 2008, **93**, 192914.
18 T. Hoshina, *J. Ceram. Soc. Jpn.*, 2013, **121**, 156–161.
19 V. Buscaglia and C. A. Randall, *J. Eur. Ceram. Soc.*, 2020, **40**, 3744–3758.
20 R. Eglitis, G. Borstel, E. Heifets, S. Piskunov and E. Kotomin, *J. Electroceram.*, 2006, **16**, 289–292.
21 R. Eglitis and D. Vanderbilt, *Phys. Rev. B: Condens. Matter Mater. Phys.*, 2007, **76**, 155439.
22 A. M. Kolpak, D. Li, R. Shao, A. M. Rappe and D. A. Bonnell, *Phys. Rev. Lett.*, 2008, **101**, 036102.
23 A. Höfer, M. Fechner, K. Duncker, M. Hölzer, I. Mertig and W. Widdra, *Phys. Rev. Lett.*, 2012, **108**, 087602.
24 J. Dionot, G. Geneste, C. Mathieu and N. Barrett, *Phys. Rev. B: Condens. Matter Mater. Phys.*, 2014, **90**, 014107.
25 T. Sun, X. Wang, H. Wang, Z. Cheng, X. Zhang and L. Li, *J. Am. Ceram. Soc.*, 2010, **93**, 3808–3813.
26 C. Fang, D. Zhou and S. Gong, *Phys. B*, 2011, **406**, 1317–1322.
27 M. Salazar-Villanueva, A. B. Hernandez, E. C. Anota, J. R. Mora, J. A. Ascencio and A. M. Cervantes, *Mol. Simul.*, 2013, **39**, 545–549.
28 R. A. Evarestov, A. V. Bandura and D. D. Kuruch, *J. Comput. Chem.*, 2013, **34**, 175–186.
29 M. B. Smith, K. Page, T. Siegrist, P. L. Redmond, E. C. Walter, R. Seshadri, L. E. Brus and M. L. Steigerwald, *J. Am. Chem. Soc.*, 2008, **130**, 6955–6963.
30 J. Zhu, W. Han, H. Zhang, Z. Yuan, X. Wang, L. Li and C. Jin, *J. Appl. Phys.*, 2012, **112**, 064110.
31 P. Sedykh and D. Michel, *Phys. Rev. B: Condens. Matter Mater. Phys.*, 2009, **79**, 134119.
32 C. Shi, S. J. Billinge, E. Puma, S. H. Bang, N. J. Bean, J.-C. de Sugny, R. G. Gambee, R. C. Haskell, A. Hightower and T. C. Monson, *Phys. Rev. B*, 2018, **98**, 085421.
33 V. Lukacs, M. Airimioaei, L. Padurariu, L. Curecheriu, C. Ciomaga, A. Bencan, G. Drazic, M. Avakian, J. Jones and G. Stoian, *et al.*, *J. Eur. Ceram. Soc.*, 2022, **42**, 2230–2247.
34 D. Ghosh, A. Sakata, J. Carter, P. A. Thomas, H. Han, J. C. Nino and J. L. Jones, *Adv. Funct. Mater.*, 2014, **24**, 885–896.
35 L. Lemos da Silva, K.-Y. Lee, S. Petrick, M. Etter, A. Schökel, C. G. Chaves, N. Oliveira da Silva, K. Lalitha, G. Picht and M. J. Hoffmann, *et al.*, *J. Appl. Phys.*, 2021, **130**, 234101.
36 F. A. Rabuffetti and R. L. Brutchey, *J. Am. Chem. Soc.*, 2012, **134**, 9475–9487.
37 Y. Hao, Z. Feng, S. Banerjee, X. Wang, S. J. L. Billinge, J. Wang, K. Jin, K. Bi and L. Li, *J. Mater. Chem. C*, 2021, **9**, 5267–5276.
38 J. Li, J. Claude, L. E. Norena-Franco, S. I. Seok and Q. Wang, *Chem. Mater.*, 2008, **20**, 6304–6306.
39 A. Dong, X. Ye, J. Chen, Y. Kang, T. Gordon, J. M. Kikkawa and C. B. Murray, *J. Am. Chem. Soc.*, 2011, **133**, 998–1006.
40 M. J. Polking, M.-G. Han, A. Yourdkhani, V. Petkov, C. F. Kisielowski, V. V. Volkov, Y. Zhu, G. Caruntu, A. P. Alivisatos and R. Ramesh, *Nat. Mater.*, 2012, **11**, 700–709.
41 D. Caruntu, T. Rostamzadeh, T. Costanzo, S. S. Parizi and G. Caruntu, *Nanoscale*, 2015, **7**, 12955–12969.
42 S. Adireddy, C. Lin, B. Cao, W. Zhou and G. Caruntu, *Chem. Mater.*, 2010, **22**, 1946–1948.
43 K. Yasui and K. Kato, *J. Phys. Chem. C*, 2013, **117**, 19632–19644.
44 J. E. Spanier, A. M. Kolpak, J. J. Urban, I. Grinberg, L. Ouyang, W. S. Yun, A. M. Rappe and H. Park, *Nano Lett.*, 2006, **6**, 735–739.
45 D. Li, M. H. Zhao, J. Garra, A. Kolpak, A. Rappe, D. Bonnell and J. Vohs, *Nat. Mater.*, 2008, **7**, 473–477.
46 K. Page, T. Proffen, M. Niederberger and R. Seshadri, *Chem. Mater.*, 2010, **22**, 4386–4391.
47 B. Jiang, T.-M. Usher, P. R. Jothi, B. Kavey, G. Caruntu and K. Page, *Chem. – Eur. J.*, 2021, **27**(32), 8365–8371.
48 T.-M. Usher, B. Kavey, G. Caruntu and K. Page, *ACS Appl. Nano Mater.*, 2020, **3**, 9715–9723.
49 U. Ruett, J. Almer, P. Kenesei, J.-S. Park, R. Osborn, Y. Ren, D. Robinson, M. Krogstad, S. Rosenkranz and X. Zhang, *et al.*, *Synchrotron Radiation News*, 2020, **33**, 44–50.
50 A. Hammersley, S. Svensson, M. Hanfland, A. Fitch and D. Hausermann, *Int. J. High Pressure Res.*, 1996, **14**, 235–248.
51 P. Juhás, T. Davis, C. L. Farrow and S. J. Billinge, *J. Appl. Crystallogr.*, 2013, **46**, 560–566.
52 A. Coehlo, *Coelho Software*, 2016.
53 T.-M. Usher, D. Olds, J. Liu and K. Page, *Acta Crystallogr., Sect. A: Found. Adv.*, 2018, **74**, 322–331.
54 B. J. Rodriguez, C. Callahan, S. V. Kalinin and R. Proksch, *Nanotechnology*, 2007, **18**, 475504.
55 G. Caruntu, A. Yourdkhani, M. Vopsaroiu and G. Srinivasan, *Nanoscale*, 2012, **4**, 3218–3227.
56 S. M. Yang, L. Mazet, M. B. Okatan, S. Jesse, G. Niu, T. Schroeder, S. Schamm-Chardon, C. Dubourdieu, A. P. Baddorf and S. V. Kalinin, *Appl. Phys. Lett.*, 2016, **108**, 252902.
57 V. Petkov, M. Gateshki, M. Niederberger and Y. Ren, *Chem. Mater.*, 2006, **18**, 814–821.
58 V. Petkov, V. Buscaglia, M. Buscaglia, Z. Zhao and Y. Ren, *Phys. Rev. B: Condens. Matter Mater. Phys.*, 2008, **78**, 054107.
59 M. Senn, D. Keen, T. Lucas, J. Hriljac and A. Goodwin, *Phys. Rev. Lett.*, 2016, **116**, 207602.

60 R. E. Cohen, *Nature*, 1992, **358**, 136–138.
61 C.-L. Jia, V. Nagarajan, J.-Q. He, L. Houben, T. Zhao, R. Ramesh, K. Urban and R. Waser, *Nat. Mater.*, 2007, **6**, 64–69.
62 C. M. Culbertson, A. T. Flak, M. Yatskin, P. H.-Y. Cheong, D. P. Cann and M. R. Dolgos, *Sci. Rep.*, 2020, **10**, 1–10.
63 R. C. Miller and A. Savage, *J. Appl. Phys.*, 1959, **30**, 808–811.
64 M. Alexe, C. Harnagea, D. Hesse and U. Gösele, *Appl. Phys. Lett.*, 2001, **79**, 242–244.
65 S. V. Kalinin, Y. Kim, D. D. Fong and A. N. Morozovska, *Rep. Prog. Phys.*, 2018, **81**, 036502.
66 T. Bastow and H. Whitfield, *Solid State Commun.*, 2001, **117**, 483–488.
67 A. Taye, G. Klotzsche, D. Michel, S. Mulla-Osman and R. Böttcher, *J. Phys.: Condens. Matter*, 1999, **11**, 871–879.
68 P. Sedykh, J. Haase, D. Michel and E. V. Charnaya, *Ferroelectrics*, 2008, **363**, 215–226.
69 P. Sedykh, D. Michel, E. V. Charnaya and J. Haase, *Ferroelectrics*, 2010, **400**, 135–143.